



Preparation and characterization of $(\text{CuInTe}_2)_{1-x}(\text{TaTe})_x$ solid solutions ($0 < x < 1$)

P. Grima-Gallardo ^{a, b, *}, O. Izarra ^a, L. Méndez ^b, S. Torres ^b, M. Quintero ^a, H. Cabrera ^{c, d}, E. Pérez-Cappé ^e, I. Zumeta-Dubé ^f, A. Rodríguez ^f, J.A. Aitken ^g, D.P. Rai ^h

^a Centro de Estudios en Semiconductores (CES), Departamento de Física, Facultad de Ciencias, Universidad de Los Andes (ULA), Mérida, Venezuela

^b Centro Nacional de Tecnología Óptica (CNTO), Mérida, Venezuela

^c SPIE-ICTP Anchor Research in Optics Laboratory, International Centre for Theoretical Physics (ICTP), Trieste, Italy

^d Centro Multidisciplinario de Ciencias, Instituto Venezolano de Investigaciones Científicas (IVIC), Mérida, Venezuela

^e Instituto de Ciencia y Tecnología de Materiales (IMRE), Universidad de La Habana, Vedado, Cuba

^f Instituto Politécnico Nacional, Centro de Investigación en Ciencia Aplicada y Tecnología Avanzada, Unidad Legaria, México D.F, Mexico

^g Department of Chemistry and Biochemistry, Duquesne University, Pittsburgh, USA

^h Department of Physics, Pachhunga University College, Aizawl, 796001, India

ARTICLE INFO

Article history:

Received 7 November 2017

Received in revised form

22 February 2018

Accepted 26 February 2018

Available online 3 March 2018

Keywords:

Alloys

CuInTe_2

TaTe

Spinodal decomposition

Magnetic susceptibility

ABSTRACT

Polycrystalline samples of the $(\text{CuInTe}_2)_{1-x}(\text{TaTe})_x$ alloys system were prepared by the melt and anneal technique in the composition range $0 < x < 1$. Products were characterized by X-Ray Diffraction (XRD), Scanning Electron Microscopy (SEM), Differential Thermal Analysis (DTA) and SQUID techniques. From XRD and SEM, it was found that the solubility of TaTe in CuInTe_2 is around 10%; however, samples up to $x = 2/3$ are composed by a mean tetragonal CuInTe_2 -like phase with traces of Ta_2Te_3 . Samples with $x > 2/3$ show diffraction patterns with several phases with poor crystallization. In addition, the tetragonal CuInTe_2 -like phase shows spinodal decomposition i.e. there are two phases, one Ta-rich and the other Ta-poor, with the same crystal structure and very close lattice parameters. SEM measurements also show up to six different phases, although they do not produce observed diffraction line in powder XRD patterns.

DC magnetic susceptibility measurements as a function of temperature using the ZFC-FC protocol were performed in samples with $x \leq 2/3$. With the exception of $x = 2/3$, all samples show a similar behavior in the ZFC and FC curves which are typical of a system with a distribution of magnetic cluster sizes. Sample $x = 2/3$ shows ferromagnetic behavior with $T_c = 50$ K. For sample $x = 1/4$, measurements of the magnetization as a function of the applied magnetic field and temperature were performed. From the analysis of the curves it was found that the clusters contain 10^5 Ta-atoms and a coercitive field of 0.22 kOe at $T = 5$ K.

© 2018 Elsevier B.V. All rights reserved.

1. Introduction

Spintronics exploits the spin of the electron rather than its charge to create a new generation of devices, which will be smaller, more versatile and more robust than those currently making up silicon chips and circuit elements [1,2]. Due to these great advantages, intensive attention has been paid to semiconductors with potential room temperature ferromagnetism (RT-FM), including

$\text{A}^{\text{II}}\text{B}^{\text{IV}}\text{C}^{\text{VI}}_2$ and $\text{A}^{\text{I}}\text{B}^{\text{III}}\text{C}^{\text{VI}}_2$ chalcopyrite semiconductors, doped or alloyed with transition metals (TMs). Most of the experimental and theoretical investigations has been based on the use of Mn as TM since the electronic structure of this element ($[\text{Ar}] 3d^5 4s^2$) looks very appropriate for the substitution of cations in the ternary matrix of chalcopyrite compounds [3–19]. Additionally, in particular for $\text{A}^{\text{I}}\text{B}^{\text{III}}\text{C}^{\text{VI}}_2$ compounds, substitution with other TMs, such as Fe, Cr, Co, Ni and Ta has been also investigated [13,20–26]. Details about alloy system investigated, included composition, preparation and magnetic behavior are show in Tables 1 and 2.

By inspection of Tables 1 and 2, it can be noted that RT-FM has only been observed in several $\text{A}^{\text{II}}\text{B}^{\text{IV}}\text{C}^{\text{VI}}_2$ compounds doped with Mn, whereas for $\text{A}^{\text{I}}\text{B}^{\text{III}}\text{C}^{\text{VI}}_2$ doped or alloyed with any TMs there are no

* Corresponding author. Centro de Estudios en Semiconductores (CES), Departamento de Física, Facultad de Ciencias, Universidad de Los Andes (ULA), Mérida, Venezuela.

E-mail address: peg@ula.ve (P. Grima-Gallardo).

Table 1
Chalcopyrite compounds doped or alloyed with Mn.

Alloys	Magnetic element composition	Synthesis method	Magnetic behavior	T _c [K]	Reference
A ^{II} B ^{IV} C ^V ₂					
Cd _{1-x} Mn _x GeP ₂	x = 0.2	SSR	FM	300	[3]
Zn _{1-x} Mn _x GeP ₂	x = 0.056	SSR	FM	312	[4]
(ZnGe) _{1-x} Mn _x As ₂	x = 5 mass %	BM	FM	333	[5]
(ZnSn) _{1-x} Mn _x As ₂	x = 1.2 mass %			329	
(CdGe) _{1-x} Mn _x As ₂	x = 6 mass %	SSR	FM	355	[6]
(ZnGe) _{1-x} Mn _x As ₂	x = 3.5 mass %	SSR	FM	367	[7]
(ZnSi) _{1-x} Mn _x As ₂	x = 1 mass %	SSR	FM	325	[8]
	x = 2 mass %			337	
Zn _{1-x} Mn _x GeAs ₂	x = 0.078	SSR	FM	320	[9]
(Zn _{0.9} Cd _{0.1}) _{1-x} Mn _x GeAs ₂	x = 1.13 mass %	SSR	FM	349	[10]
	x = 2.65 mass %			351	
AIBIIICVI ₂					
Cu _{1-x} Mn _x InTe ₂	x = 0.03 and 0.06 x = 0.09 and 0.12	SSR	PM AFM	–	[11]
(CuIn) _{1-x} Mn _{2x} Te ₂	0.010 ≤ x ≤ 0.101	BM	SG	–	[12]
CuIn _{1-x} Mn _x S _{2-x}	x = 0, 0.05, 0.1 and 0.2	SSR	AFM	–	[13]
Cu _{x/2} In _{x/2} Mn _x S ₂	x = 0.1				
CuIn _{1-x} Mn _x S ₂	x = 0–0.2	SSR	PM	–	[14]
Cu _{1-x} Mn _x InS ₂	x = 0–0.1				
Cu _{1-x} Mn _x InS ₂	x = 0–0.20	SSR	PM	–	[15]
Cu _{0.95-x} Mn _{0.05} InSe ₂					
CuIn _{1-x} Mn _x Se ₂	x = 0.0125–0.2	SSR	PM	–	[16]
Cu _{1-y} In _{1-y} Mn _{2y} Se ₂	2y = 0.0125–0.6				
Cu _{x/2} Ga _{x/2} Mn _x Te ₂	x = 0.2	SSR	SPM	–	[17]
Cu _{1-x} Mn _{2x} InS ₂	x = 0.03	SSR	PM + FM	–	[18]
Cu _{1-x} Mn _{2x} AlS ₂	x = 0.01				
CuGa _{1-x} Mn _x Te ₂	x = 0.004, 0.008, 0.010 and 0.012	SSR	SPM	–	[19]

T_c: critical temperature (magnetic transition temperature from paramagnetic to ferromagnetic).

SSR: Solid State Reaction; BM: Bridgman Method; PM: Paramagnetic; AFM: Antiferromagnetic; SG: Spin Glass; SPM: Superparamagnetic; FM: Ferromagnetic.

Table 2
A^IB^{III}C^{VI}₂ compounds doped or alloyed with TMs different than Mn.

Alloys	Magnetic element composition	Synthesis method	Magnetic behavior	T _c [K]	Ref.
CuIn _{1-x} Fe _x S ₂	x = 0.1	SSR	AFM	–	[13]
(CuIn) _{1-x} Fe _x Te _{2-x}	x = 0.5	SSR	SPM	–	[20]
(CuGa) _{1-x} Fe _x Te _{2-x}					
(CuIn) _{1-x} Fe _x Se _{2-x}	x = 0.5	SSR	SPM	–	[21]
(CuAl) _{1-x} Cr _x S _{2-x}	x = 0.1 and 0.2	SSR	AFM	–	[22]
	x = 0.33				[23]
(CuIn) _{1-x} Co _x Te _{2-x}	x = 0.67	SSR	SPM	–	[24]
(CuIn) _{1-x} Ni _x Te _{2-x}			DM + FM		
(CuIn) _{1-x} Ta _x Te _{2-x}	x = 0.25	SSR	SPM	–	[25]
(CuIn) _{1-x} Ta _x Se _{2-x}	x = 0.25	SSR	SG	50	[26]
(CuIn) _{1-x} Ta _x Te _{2-x}	x = 2/3		FM		

SSR: Solid State Reaction; DM: Diamagnetic; AFM: Antiferromagnetic; SG: Spin Glass; SPM: Superparamagnetic; FM: Ferromagnetic. T_c: critical temperature (transition temperature from paramagnetic to ferromagnetic).

reports of RT-FM.

RT-FM is thought to arise from the interaction of holes (created by substitution of B^{IV} or B^{III} cations) with the local moment of the *d* electrons of TMs²⁺ [27,28]; however it is also argued that it is due by the presence of magnetic secondary phases such as MnP and MnAs [28–32]. Kochura et al. (2013), in samples prepared by solid state reaction under the condition of fast cooling, found that there exist three types of magnetic species in A^{II}B^{IV}C^V₂: Mn alloys: a) substitution of Mn ions making Mn complexes (especially dimers), b) MnAs micro-precipitates and c) MnAs nanosize precipitates (clusters with a mean diameter of 3 nm) [29].

Although the origin of RT-FM is until now under investigation, it seems well established that the magnetic behavior in A^{II}B^{IV}C^V₂: Mn alloys is composition dependent: at low values of x, the alloy shows a typical paramagnetic behavior (or also superparamagnetic) [6,8] whereas for higher values of x, a critical x_c value is attained for which, the paramagnetic→ferromagnetic transition occurs. It is also worth to note here that T_c values are approximately the same

for all A^{II}B^{IV}C^V₂: Mn alloys suggesting that this transition is related to Mn-based secondary phases more than substitution of cations for Mn²⁺ in the ternary matrix.

It is interesting to compare experimental results with those obtained by theoretical calculations. Katamani et al. (2003) [33,34] using KKR-CPA-LDA method predict that ferromagnetic states are stable in (Cd_{1-x}V_x)GeP₂ and (Cd_{1-x}Cr_x)GeP₂, alloys whereas (Cd_{1-x}Mn_x)GeP₂, (Cd_{1-x}Fe_x)GeP₂ and (Cd_{1-x}Co_x)GeP₂ alloys must show spinglass-like ground states (calculations were made using x = 0.1); Ti and Ni substitutions in CdGeP₂ could not have a net magnetic moment (the same are applicable to ZnGeP₂ and CdSiAs₂). On the other hand, the ferromagnetic state was found to be stable in AgGaS₂ (CuAlS₂) doped with Ti, V, Cr and Mn, whereas doping with Fe, Co and Ni must stabilize a spinglass-like state. The work of Zhao et al. (2004) [35], using first principle calculations, coincides with Katamani and predicts that Mn doping at the III site in A^IB^{III}C^{VI}₂ compounds provides holes that must stabilize ferromagnetic coupling between Mn ions. The predictions of both works

(Katamani and Zhao) are contradictory to that which has been observed experimentally! The reason for the discrepancies between theoretical expectations and experimental results is not clear until now. It has been suggested, that stabilization of ferromagnetism is also due to the interaction of holes with Mn magnetic moments but induced by: a) intrinsic defects [36,37]; b) non-uniform spatial distribution of carriers and/or and magnetic ions [38]; or c) nanoscale phase separation driven either by randomness in the carrier and spin subsystems or by limited solubility of transition metals in the host semiconductor, which leads to spinodal decomposition into regions with a small and a large concentration of the magnetic constituents [38]. It is evident that additional experimental work, in greater variety of systems and with larger concentration of the transition metal dopant, is necessary.

In this work, we report the preparation, X-ray diffraction (XRD), differential thermal analysis (DTA), scanning electron microscopy (SEM) and magnetic measurements using SQUID technique of the $(\text{CuInTe}_2)_{1-x}(\text{TaTe})_x$ alloy system, in the composition interval $0 < x < 1$. Some partial results have been published previously: a preliminary report of XRD measurements and calculated lattice parameters have been presented in a conference [39], the crystal structure of composition $x = 2/3$ analyzed by Rietveld refinement [52] and the magnetic behavior of samples $x = 1/4$ [25] and $x = 2/3$ [26]. However, some characteristics of this alloy system remain unclear. The diffractions patterns show a mean chalcopyrite-like phase in the composition interval $0 \leq x \leq 2/3$ with only traces of secondary phases when it is expected that Ta must have a relative low solubility in CuInTe_2 . Where has the Ta gone? Is it in the CuInTe_2 matrix? It is segregate at the grain boundaries or does it forms no-crystalline phases? Under a more exhaustive examination of the diffraction patterns we have observed some satellite peaks around the stronger 112-peak, characteristic of the chalcopyrite structure, the presence of which have been explained in this work on the basis of a spinodal decomposition. Also, in this work we have added SEM measurements trying to elucidate what's happens with Ta. Finally we report DC magnetic susceptibilities for all studied compositions and M Vs H measurements for composition $x = 0.25$ in order to obtain the number of Ta atoms for magnetic cluster and basic parameters (magnetic saturation, magnetic remanence and coercitive field).

2. Experimental procedure

2.1. Preparation of the samples

The samples were synthesized using the melt and annealing technique as described elsewhere [40]. Stoichiometric quantities of the elements with purity of 99.99% were charged in a synthetic silica glass ampoule, which was previously subject to pyrolysis in order to avoid reaction of the starting materials with silica glass. Then, the ampoule was sealed under vacuum ($\sim 10^{-4}$ Torr) and the fusion process was carried out inside a furnace (vertical position) heated up to 1500 K at a rate of 20 K/h, with a stop of 48 h at 723 K (melting point of Te). The ampoule was shaken using a mechanical system during the entire heating process in order to guarantee the complete mixing of all the elements and the formation of binary species at low temperature. Then, the temperature was gradually decreased until 600 K and this temperature was maintained for 60 days. Finally, the sample was cooled to room temperature by switching off the furnace.

2.2. X-ray diffraction (XRD)

A small quantity of each sample, cut from the center of the ingot, was ground mechanically in an agate mortar and pestle. The

resulting fine powder, sieved to 106 μm , was mounted on a flat zero-background holder covered with a thin layer of petroleum jelly. The X-ray powder diffraction data were collected at ambient temperature (298 K) in θ/θ reflection mode using a Siemens D5005 diffractometer equipped with an X-ray tube (Cu $K\alpha$ radiation: $\lambda = 1.54059$ Å; 40 kV, 30 mA) and equipped with Ge(111) primary monochromator. A fixed aperture and divergence slit of 1 mm, a 1 mm monochromator slit, and a 0.1 mm detector slit were used. The specimen was scanned from 10–100° in 2θ , with step size of 0.02° and counting time of 40 s. Quartz was used as an external standard. The Bruker AXS analytical software was used to establish the position of the peaks.

2.3. Differential thermal analysis (DTA)

Phase transition temperatures were obtained from differential thermal analysis measurements using Perkin-Elmer DTA-7 with gold as a reference material. The charge was an approximately 100 mg powdered alloy. Values of the transitions for the materials were obtained from the peaks on the DTA. Each phase transition temperature value was determined from the base line intercept of the tangent to the leading edge of the peak in the difference signal. Both, heating and cooling runs, were carried out for each sample, the average rate of these runs being approximately 10 K/min. The error in determining absolute temperatures is about ± 8 K.

2.4. Scanning electron microscopy (SEM)

The stoichiometric ratios of the samples were investigated by SEM technique, using a FE-8 SEM, Jeol 6301-F equipment. The micro-chemical composition was found using an energy dispersive X-ray spectrometer (EDS) coupled with a computer-based multi-channel analyzer (MCA), (Delta III analysis and Quantex software, KeveX). For the EDS analysis $K\alpha$ lines were used. Accelerating voltage was 15 kV. The samples were tilted by 35°. A standardless EDS analysis was made with a relative error of $\pm 5\%$ and detection limits of the order of 0.3 wt%, where the k -ratios were based on theoretical standards.

2.5. Magnetic characterization

DC magnetic susceptibility and magnetization as a function of the applied field and temperature measurements were performed on a Quantum Design SQUID magnetometer, equipped with a superconducting magnet able to produce fields up to 5 T. The samples in the form of powder were compacted with a piece of cotton inside the sample holder in order to prevent any movement. Zero-field-cooling and field cooling (ZFC-FC) measurements were carried out in the temperature range of 2–300 K.

3. Results and discussion

3.1. X-ray diffraction (XRD)

X-ray diffraction patterns for the $(\text{CuInTe}_2)_{1-x}(\text{TaTe})_x$ alloys system are displayed in Fig. 1. For $x = 0$ (CuInTe_2) the diffraction pattern was simulated using Powder Cell software [41] and the lattice parameters $a = 6.1944$ Å, $c = 12.4157$ Å, reported by Knight et al. [42].

We used fractions for the composition values, because it is well known in chemistry that, if intermediate compounds exist in the phase diagram, generally they are correlated with relations between integer values of each of the compounds that make up the alloy. We can observe in Fig. 1 that, at first sight, for compositions from $x = 1/8$ to $x = 2/3$, the diffraction patterns have in common the

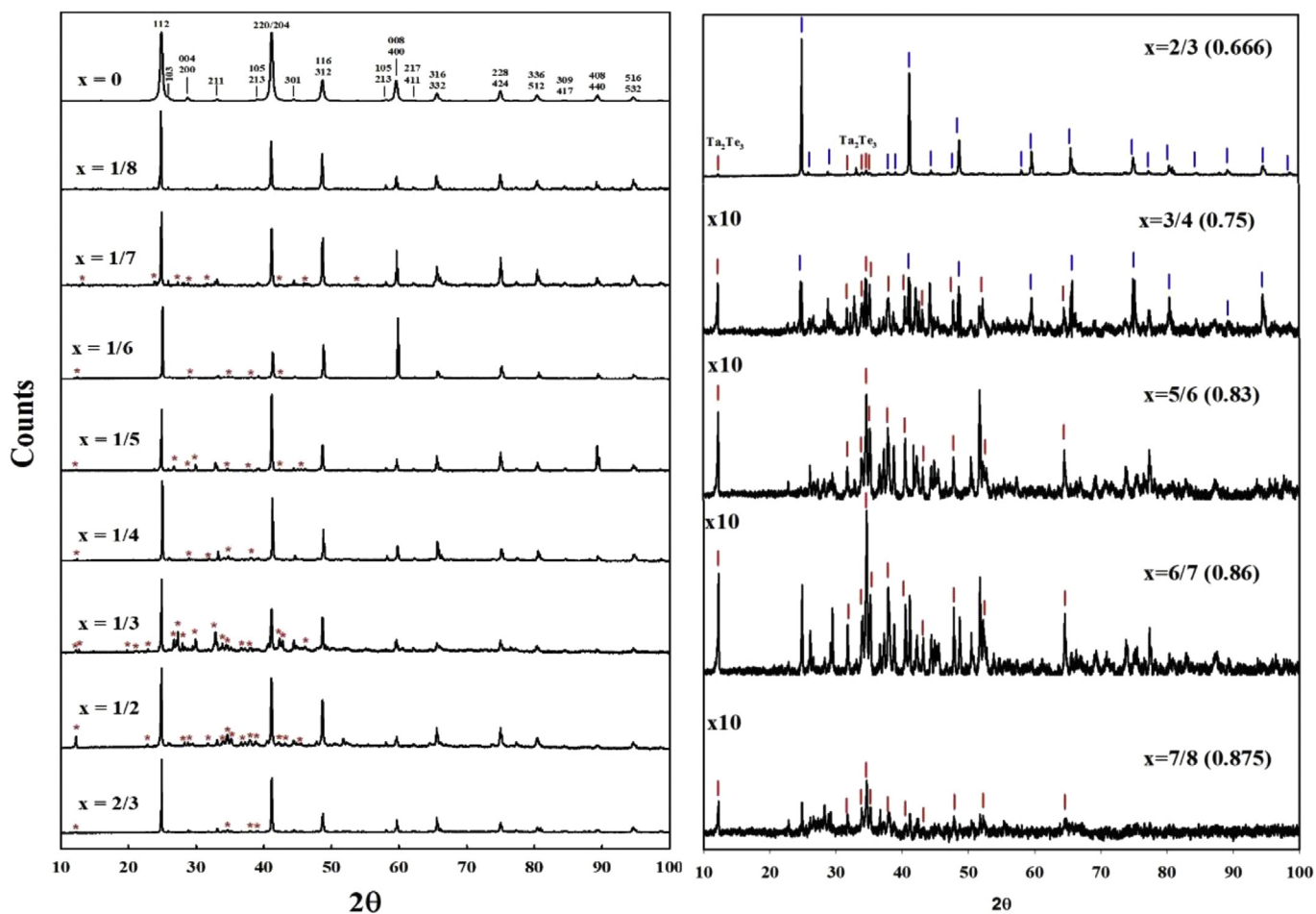


Fig. 1. X-ray diffraction patterns for the $(\text{CuInTe}_2)_{1-x}(\text{TaTe})_x$ alloys system. Left side: compositions from $x=0$ to $x=2/3$ (red asterisks signals secondary phases). Right side: compositions from $x=2/3$ to $x=7/8$ (red and blue traits identifies Ta_2Te_3 and CuInTe_2 -like phases, respectively). The intensity of the peaks for compositions from $3/4$ to $7/8$ have been multiplied by a factor 10. (For interpretation of the references to colour in this figure legend, the reader is referred to the Web version of this article.)

presence of a mean tetragonal CuInTe_2 -like phase accompanied by traces of secondary phases (signaled by asterisks) whereas for compositions from $x=3/4$ to $x=7/8$ the samples show very poor crystallization and seem to be composed by an admixture of phases, one of them has been identified as Ta_2Te_3 whereas some others peaks belong to unknown phases. The relative intensity of the stronger diffraction peaks for the CuInTe_2 -like phase varies for different compositions. This fact suggests that Ta, which has a mass attenuation coefficient equal to $180.95 \text{ cm}^2/\text{g}$ for $\text{CuK}\alpha$ radiation in comparison with 63.546 and $114.82 \text{ cm}^2/\text{g}$ for Cu and In respectively, occupies at random the 4a and 4b cationic sites of the original tetragonal chalcopyrite-like structure since we cannot observe a regular behavior for the variation of the intensities of the diffraction peaks. The I symmetry of CuInTe_2 (space group $I\bar{4}2d$), given by the fact that Te-atoms are located at the center of a tetrahedral configuration surrounded by 2 Cu and 2 In atoms, is broken by partial substitution with Ta-atoms, giving rise to a P symmetry with an increment of the crystallographic sites. In a previous work we reported that the alloy CuTaInSe_3 , which corresponds to $x=0.5$ for the $(\text{CuInTe}_2)_{1-x}(\text{TaTe})_x$ alloys system, crystallizes in a tetragonal chalcopyrite-like structure, space group $P\bar{4}2c$, with Cu, Ta and In in 2c, 2e and 2b sites, respectively, with site occupation factors equal to 1, whereas the 2f sites are shared by the three cations at random with site occupation factors of $1/3$ for each [43]. In general, the effect of substitution of Cu and/or In cations by

a transition metal in these alloys, give rise to a series of successive phase transitions from the ordered chalcopyrite phase ($x=0$) s.g. $I\bar{4}2d$ to a semi-ordered chalcopyrite-like phase s.g. $P\bar{4}2c$ for

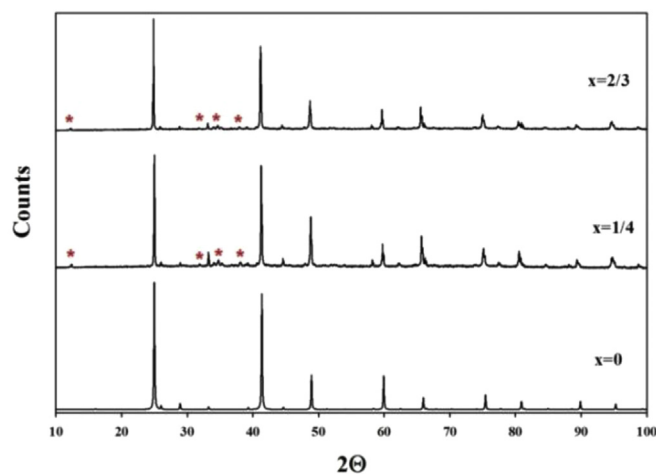


Fig. 2. X-ray diffraction patterns for compositions $x=0$ (calculated), $1/4$ and $2/3$ (experimentals) in the $(\text{CuInTe}_2)_{1-x}(\text{TaTe})_x$ alloys system. Asterisks identify the secondary phase Ta_2Te_3 .

intermediary values of x and again to a reordered stannite-like structure s.g. $\sqrt{42}m$ for $x = 2/3$ [44].

In Fig. 2, for a closer comparison, the calculated diffraction pattern of CuInTe_2 and with compositions $x = 1/4$ and $2/3$, are shown.

It is a little unexpected and surprising that at such high values of x as $2/3$, the diffraction patterns are composed by a main tetragonal chalcopyrite-like phase and barely traces of a secondary phase. Observing more attentively the diffraction patterns we can notice that the strongest peak (the 112-hkl) of the mean phase shows a shoulder at its right side and several other structures at the left side (see Fig. 3).

Let us first to explain the shoulder at the right side. Fig. 4 shows the positions of the 112-peak and shoulder as a function of composition.

The positions of the 112-diffraction peaks are nearly constant with the exception of $x = 1/8$ which is a little lower but in the limits of the experimental error (estimated in ± 0.05 in 2θ) and compositions $x = 1/6$ and $1/4$ which values are 0.6% higher (three times the experimental error) possibly due to disorder. The position of the shoulder (white circle) is located always a little higher in 2θ for all compositions. In the inset, the differences in 2θ between the 112-diffraction peak and the shoulder, labeled as delta, are given. It is worth to note that these differences are constant for all compositions. This is typical for spinodal nanodecomposition, i.e. the formation of two different phases, one of them rich in Ta and the other poor, with the same crystal structure and very close lattice parameters.

In Fig. 5, the calculated lattice parameters, a and c , using DICVOL 06 software [45] are shown.

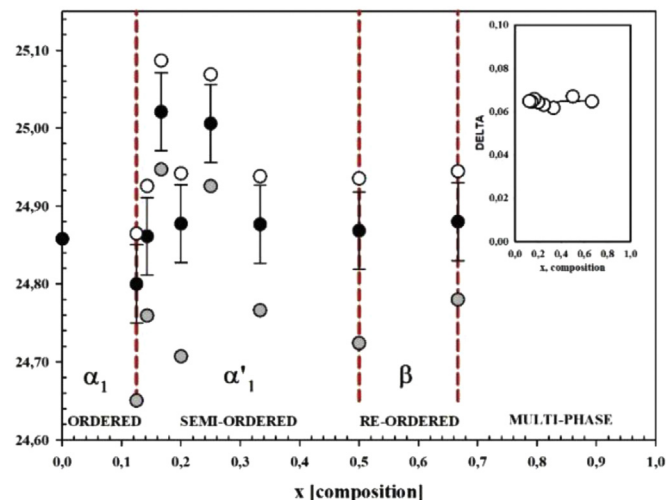


Fig. 4. The 2θ position of the 112-diffraction peak (black circles), its right-side shoulder (white circles), and in the inset, the difference between both positions as a function of the composition x (the solid line is a linear regression over the experimental points). The estimated error in 2θ is given only for the black circles to avoid overcrowding the figure. The red dash lines give the approximate limits for the phase fields labeled as α (ordered), α' (semi-ordered), and β (re-ordered) according to [44]. (For interpretation of the references to colour in this figure legend, the reader is referred to the Web version of this article.)

Analyzing the 2θ values of the strongest peak (black circles) we can observe that the parameter a increases from $x = 0$ to $x = 1/8$ and then remains nearly constant inside the limits of the

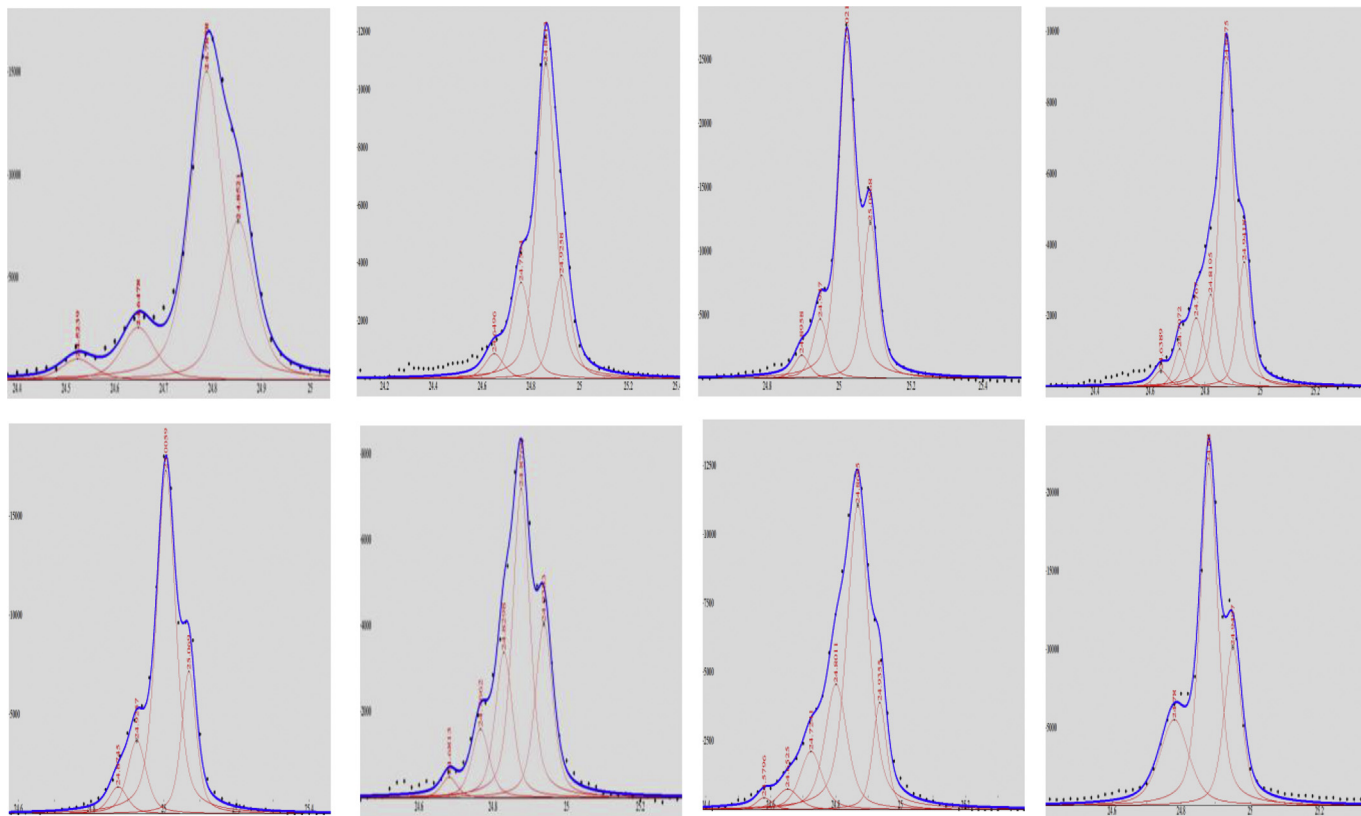


Fig. 3. Fit of the strongest x-ray diffraction peak (112-hkl) for compositions $x = 1/8, 1/7, 1/6, 1/5, 1/4, 1/3, 1/2$ and $2/3$ (from left to right and from top to bottom). Black circles: experimental points; blue line: fit with pseudo-Voigt curves (in red). The labels give the respective 2θ values. (For interpretation of the references to colour in this figure legend, the reader is referred to the Web version of this article.)

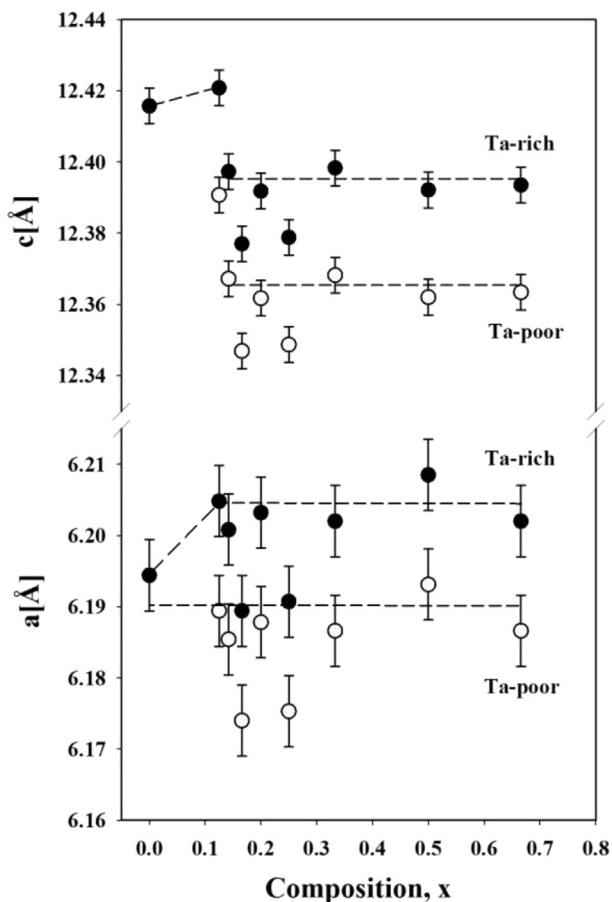


Fig. 5. Calculated lattice parameters for the $(\text{CuInTe}_2)_{1-x}(\text{TaTe})_x$ alloys system. Black circles: Ta-rich phase. White circles: Ta-poor phase. The dashed lines don't have particular physical meaning and only are included as an aid for the explanation in the text.

experimental error (excluding compositions $x = 1/6$ and $x = 1/4$), whereas the 2θ values of the shoulder remain nearly constant in the entire composition range (excluding again samples $x = 1/6$ and $x = 1/4$). This behavior suggests that the solubility of Ta in the ternary matrix is on the order of 10% obtained from the crossover of the dashed lines for black circles. The covalent radii tables of the elements vary from one author to another, Ta varies from 1.34 to 1.38 Å, Cu goes from 1.17 to 1.38 Å and In from 1.44 to 1.50 Å [46–51]. The observed increase in the parameter a suggests that Ta-atoms preferentially occupy the Cu-atom sites since the covalent radius of Ta is lower than that of In. If Ta-atoms go to the In-atoms sites, it is expected that the lattice parameter a must decrease, as it is the cases of samples $x = 1/6$ and $x = 1/4$! This fact could give credit to our previous assertion, based on the relative intensities of the diffraction peaks, that Ta-atoms would substitute Cu or In-atoms at random.

With respect to the 2θ positions of the structures at left side of the 112-peak, some regularity can be observed but not enough to achieve definitive conclusions: a) not all the structures all observed for all the compositions; b) the 2θ values of the observed structures do not match with some possible binary Ta-Te reported compounds; c) it is not possible to establish unambiguously if the 2θ values of each structure increases, decreases or remains constant with composition since the variations are lower than the experimental error; and d) the presence of other binary or ternary phases, including oxides, cannot be discarded.

3.2. Scanning electron microscopy (SEM)

In addition, in order to have a better understanding of the phases present in this alloy system, scanning electron microscopy (SEM) measurements were performed in samples $x = 1/3$, $1/4$ and $1/5$. The results are displayed in Table 3. Effectively, up to six different phases have been observed (please, see Fig. 5, Table 3 and explanation below).

3.2.1. Identification of the observed phases

α_1 is the main phase observed in the diffraction patterns up to $x = 2/3$ and contains Ta in proportions from 0.02 to 9.22% which confirms that the maximum solid solubility of TaTe in CuInTe_2 is ~10%. Its diffraction pattern is close to CuInTe_2 but with variations in the intensity relations between diffraction peaks indicative of the substitution of Cu and/or In by Ta as it was discussed in section 3.1.

The α_2 phase belongs to the Cu-Ta-Te ternary system. For its stoichiometry $(\text{Cu}_2\text{Ta}_3\text{Te}_5)$ this alloy lies in the $(\text{CuSe})_{1-x}(\text{TaTe})_x$ tie line with $x = 0.6$ (or $3/5$). In our knowledge, for this tie line, only the cubic sylvanite Cu_3TaTe_4 ($x = 1/4$) has been reported [52,53]; then, $\text{Cu}_2\text{Ta}_3\text{Te}_5$ could be a new phase in the $(\text{CuSe})_{1-x}(\text{TaTe})_x$ alloy system.

Preparation and crystal structure of α_3 phase (Ta_2Te_3) has been previously reported [54]; it is a layered compound that crystallizes in a monoclinic structure, space group $C2/m$ (12) which has been evaluated as alkali metal intercalation hosts in lithium and sodium electrochemical cells [55]. Their magnetic order has not been investigated until now.

The stoichiometry of the α_4 phase correspond to the composition $x = 2/3$ in the $(\text{CuInTe}_2)_{1-x}(\text{TaTe})_x$ alloy system. The crystal structure of this phase has been studied previously by Rietveld refinement, where it has been found that this alloy crystallizes in a tetragonal stannite structure, space group $I\bar{4}2m$ (121) [56]. It shows a ferromagnetic behavior with $T_c \sim 50$ K [26].

The stoichiometry of the α_5 phase corresponds to the reported $\text{Ta}_{2.32}\text{O}_{7.40}$ compound [57,58]. It crystallizes in a layered hexagonal structure, space group $P6/mmm$ (191). Authors report “that the structure of this phase is pseudolayer due to differences in the population of atomic positions; mixed layers of Ta and O atoms alternate with purely oxygen layers”, and “a rather broad variation of the composition within the limits of one space”.

The stoichiometry of α_6 phase is close to the reported $\text{Ta}_2\text{Te}_2\text{O}_9$ compound [59–61]. This compound crystallizes in a layered monoclinic structure, space group $P2_1/c$ (14) and belongs to the $(\text{Ta}_2\text{O}_5)_{1-x}(\text{TeO}_2)_x$ tie line with $x = 1/2$ [61].

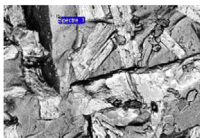
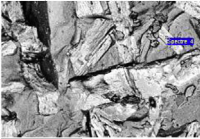
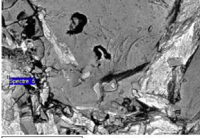
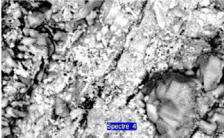
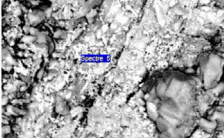
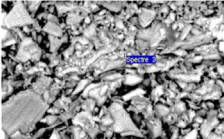

3.2.2. Presence of oxides in some samples

Although in our laboratory we follow an accurate protocol for the preparation of samples product of more than forty years of experience, for some samples we are clearly obtained the presence of oxides. Routinely we clean the pure elements with diluted $\text{HNO}_3 + \text{HF}$ solutions and then rinse in deionized water previously to be weighted and encapsulated in the quartz ampoules. We are not observed any cracking of the ampoules during the melt or thermal anneal process. However, contamination with O_2 must be occurs in one of the preparation process.

3.3. Differential thermal analysis (DTA)

Thermograms for the $(\text{CuInTe}_2)_{1-x}(\text{TaTe})_x$ alloy system are displayed in Fig. 6. It is well known that CuInTe_2 ($x = 0$) presents two-phase transitions: an order-disorder from the ordered chalcopyrite to the disordered sphalerite at 945 K, and melting at 1062 K [62]. In Fig. 6, it can observe that only composition $x = 1/8$ show phase

Table 3
Microphotographs and measured stoichiometry for compositions $x = 1/3, 1/4$ and $1/5$.

Composition and microphotographs	Code	Cu at%	In at%	Te at%	Ta at%	Phase	
$x=1/3$							
α_1 	Nominal Composition	20.0	20.0	50.0	10.0	$(\text{CuIn})_2\text{TaTe}_5$	
	E1	24.5	24.6	49.5	1.4	$\alpha_1: \sim\text{CuInTe}_2$	
	E2	26.1	24.3	49.2	0.4	$\alpha_1: \sim\text{CuInTe}_2$	
	E3	26.6	24.9	48.2	0.3	$\alpha_1: \sim\text{CuInTe}_2$	
	E7	27.2	25.1	47.7	0.0	$\alpha_1: \sim\text{CuInTe}_2$	
	E8	29.7	23.8	46.1	0.4	$\alpha_1: \sim\text{CuInTe}_2$	
	E9	24.5	24.2	50.4	0.9	$\alpha_1: \sim\text{CuInTe}_2$	
	E4	17.9	1.1	51.9	29.2	$\alpha_2: \sim\text{Cu}_2\text{Ta}_3\text{Te}_5$	
	E5	17.9	0.4	52.3	29.4	$\alpha_2: \sim\text{Cu}_2\text{Ta}_3\text{Te}_5$	
	E6	18.2	2.1	50.7	29.0	$\alpha_2: \sim\text{Cu}_2\text{Ta}_3\text{Te}_5$	
α_2 	E10	2.8	0.3	57.7	39.2	$\alpha_3: \sim\text{Ta}_2\text{Te}_3$	
α_3 							
	$x=1/4$						
	α_4 	Nominal Composition	21.4	21.4	50.0	7.1	$(\text{CuIn})_3\text{TaTe}_7$
		E1	23.6	26.5	49.9	0.0	$\alpha_1: \sim\text{CuInTe}_2$
		E2	24.2	25.2	49.6	1.0	$\alpha_1: \sim\text{CuInTe}_2$
		E3	22.8	26.2	50.3	0.7	$\alpha_1: \sim\text{CuInTe}_2$
		E4	24.5	25.9	49.4	0.2	$\alpha_1: \sim\text{CuInTe}_2$
		E5	24.0	25.7	48.8	1.5	$\alpha_1: \sim\text{CuInTe}_2$
		E6	24.2	25.6	48.7	1.5	$\alpha_1: \sim\text{CuInTe}_2$
		E9	20.1	23.7	47.0	9.2	$\alpha_1: \sim\text{CuInTe}_2$
E7		11.6	14.6	49.5	24.8	$\alpha_4: \sim\text{CuTa}_2\text{InTe}_4$	
E10		72.1(O at%)		1.6	26.1	$\alpha_5: \sim\text{Ta}_{2.32}\text{O}_{7.40}$	
α_5 	E8	68.0(O at%)		4.5	27.5	$\alpha_5: \sim\text{Ta}_{2.32}\text{O}_{7.40}$	
$x=1/5$							
α_4 	Nominal Composition	22.2	22.2	50.0	5.6	$(\text{CuIn})_4\text{TaTe}_9$	
	E1	13.9	14.4	52.1	20.0	$\alpha_4: \sim\text{CuTa}_2\text{InTe}_4$	
	E3	11.7	10.8	55.2	22.2	$\alpha_4: \sim\text{CuTa}_2\text{InTe}_4$	
	E7	63.3(O at%)		20.6	16.1	$\alpha_6: \sim(\text{TaTe})_2\text{O}_9$	
	E8	63.7(O at%)		20.9	15.5	$\alpha_6: \sim(\text{TaTe})_2\text{O}_9$	
	E9	63.6(O at%)		20.6	15.8	$\alpha_6: \sim(\text{TaTe})_2\text{O}_9$	
	E10	63.6(O at%)		20.7	15.7	$\alpha_6: \sim(\text{TaTe})_2\text{O}_9$	
	E2	55.9(O at%)		27.5	16.6	$\alpha_6: \sim(\text{TaTe})_2\text{O}_9$	
	E4	63.9(O at%)		20.4	15.7	$\alpha_6: \sim(\text{TaTe})_2\text{O}_9$	
	E5	63.1(O at%)		21.1	15.8	$\alpha_6: \sim(\text{TaTe})_2\text{O}_9$	
α_6 	E6	62.4(O at%)		18.8	18.8	$\alpha_6: \sim(\text{TaTe})_2\text{O}_9$	

Note: The sum of the percentages does not always add exactly 100% by approximations of the decimals.

transitions temperatures analogous to CuInTe_2 , at 935 and 1033 K, with one additional peak at 742 K (all values in the heating cycle) that is possible due to the presence of a third cation in the cationic sublattice. For all other compositions, the thermograms are quite different.

The solubility of TaTe in CuInTe_2 (at 600 K, the anneal temperature) in agreement with X-ray diffraction measurements, is found to be in the range 12.5 and 14.2% since the phase transition from the ordered α_1 -phase to the semi-ordered α'_1 -phase is observed between compositions $1/8$ (0.125) and $1/7$ (0.142). To simplify the discussion in the next paragraphs we will take the mean value of $x = 0.133$ for the limit of solubility.

The thermograms of samples $x = 1/7, 1/6, 1/4$ and $1/3$ show

similar thermal behavior: a little peak at very high temperatures (melting point), a wide solid + liquid region with several thermal transitions and, in the cooling cycle, the strongest peak at low temperature. This behavior is very difficult for interpretation in the absence of x-ray diffraction at high temperatures.

Sample $x = 0.5$ shows only a little peak in the heating cycle and a double little peak in the cooling. As the area under the peaks is related with the enthalpy of the thermal transition, sample $x = 0.5$ seems to be very unstable or could be a "bad" sample since the shape of the thermogram for samples $x = 1/6$ and $x = 1/4$ are very similar.

Samples $x = 1/2$ and $x = 2/3$ also shows wide solid + liquid regions with several thermal transitions but we do not observe any

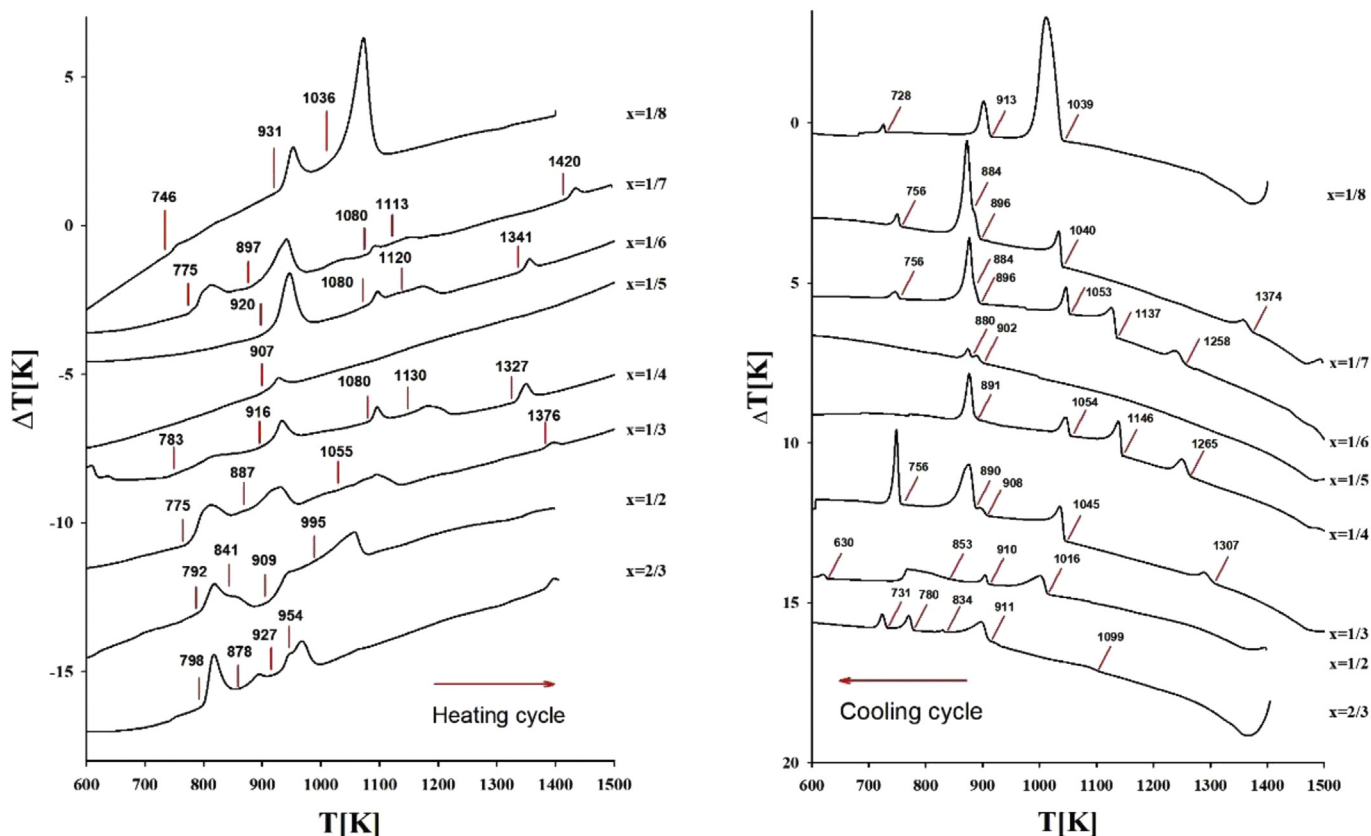


Fig. 6. Thermograms for the $(\text{CuInTe}_2)_{1-x}(\text{TaTe})_x$ alloy system. Left side: heating cycle. Right side: cooling cycle.

peak at high temperature but it is possible that the high temperature peak occurs at temperatures out of the limit of DTA furnace (~ 1500 K). Usually, we don't use the limit temperature because shortens the life of expensive thermocouples.

3.4. Magnetic measurements

DC-magnetic susceptibility (χ) as a function of temperature (T) measurements were performed in a SQUID apparatus using the well-known ZFC-FC protocol. In Fig. 7, χ Vs T curves are shown. From compositions from $x = 1/8$ to $1/2$, the $\chi(T)$ curves show a very close behavior. The observed hysteresis is typical of systems with presence of magnetic nanoclusters and the absence of a single peak in the ZFC curve (which is indicative of a unique blocking temperature) suggest a distribution of cluster sizes. The ZFC curves have, at the lower temperature (~ 2 K), the lower magnetization value as it was expected for virgin samples where the magnetic moments are oriented at random. As temperature increases the magnetization also increases due to the successive unblocking of the magnetic clusters, until they reach a plateau, at $T \sim 30$ – 50 K, indicative that the majority of clusters have been unblocked; then, the magnetization continues to increase, slowly, until the rest of the clusters unblocks. The FC curves show a flat behavior in the temperature region near $T = 300$ K whereas at low temperatures it can be observed a little increase of magnetization surely due to the presence of a weak paramagnetic component. We can conclude that for compositions from $x = 1/8$ to $1/2$, the samples contain two magnetic components, one paramagnetic (or superparamagnetic) and another ferromagnetic with $T_c > 300$ K. A change in the magnetic behavior clearly occurs between compositions $x = 1/2$ and $x = 2/3$. The sample $x = 2/3$ shows a paramagnetic \rightarrow ferromagnetic

transition at $T_c \approx 50$ K, whereas for $T < 50$ K it can be observed an increase in the magnetization due to the presence of a paramagnetic component. This change in the magnetic behavior can be attributed to the reordering of the crystal structure from the disordered chalcopyrite-like to the ordered stannite structure.

The $\chi(T)$ measurements generally were performed at low applied magnetic field (H) because of the paramagnetic and diamagnetic components increases linearly (in absolute value) with H and could mask other weak magnetic components. In our case, for measurements of Fig. 7, we used values of H from 0.2 to 0.5 kOe (see the insets of Fig. 7). However, for sample $x = 1/4$, $\chi(T)$ has been also measured using $H = 2.5$ kOe, to illustrate the previous comment (see Fig. 9). Effectively, it can be observed in Fig. 8 that with $H = 2.5$ kOe, the ZFC curve is dominated for a diamagnetic component whereas the FC curve has a weak constant positive value (please, compare with the magnetic susceptibility of sample $x = 1/4$ showed in Fig. 7 measured at $H = 0.5$ kOe).

Also, for sample $x = 1/4$, the magnetization was measured as a function of H and T. The respective curves, displayed in Fig. 9, show the coexistence of ferromagnetic and diamagnetic components. At low magnetic field, the diamagnetic component has a low value and the ferromagnetic component dominates, whereas that at higher magnetic field the diamagnetic component is imposed on the ferromagnetic component. It is worth to note also that curves at 20 K and 50 K seem to be inverted possibly due to the change in the magnetic regimen at $T \sim 50$ K observed in $\chi(T)$ measurements (Fig. 7).

From Molecular Field Theory [63], the $M(H, T)$ curves of Fig. 9 can be fitted with the equation:

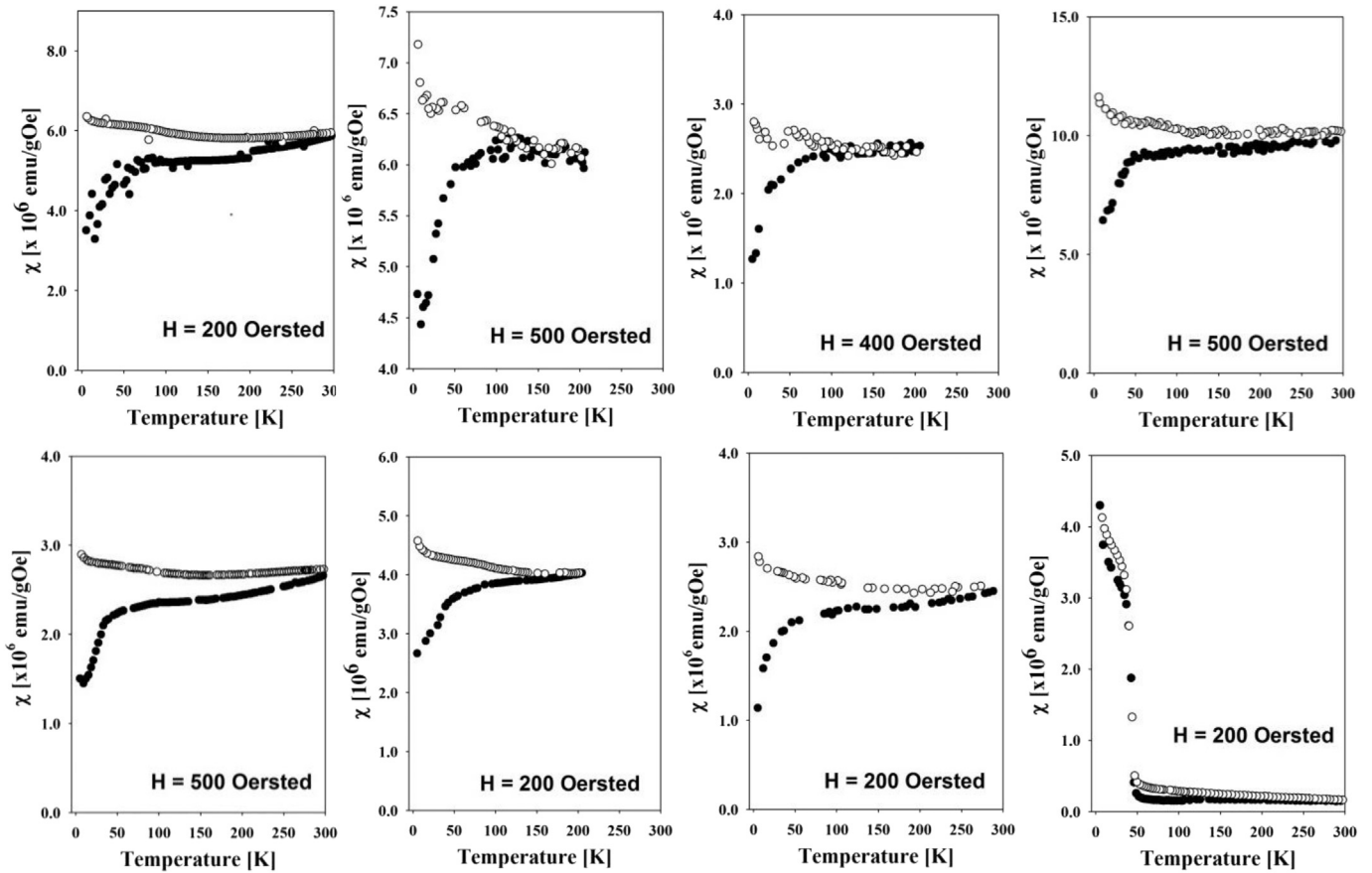


Fig. 7. DC magnetic susceptibilities as a function of temperature for the $(\text{CuInTe}_2)_{1-x}(\text{TaTe})_x$ alloy system. Top to bottom and left to right: $x = 1/8, 1/7, 1/6, 1/5, 1/4, 1/3, 1/2$ and $2/3$. White circles: Field Cooling (FC) cycle; black circles: Zero Field Cooling (ZFC) cycle.

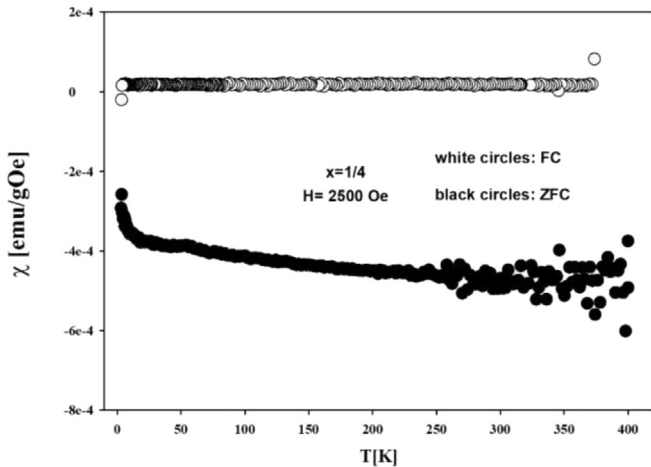


Fig. 8. $\chi(T)$ of sample $x = 1/4$ using an applied magnetic field of $H = 2.5$ kOe.

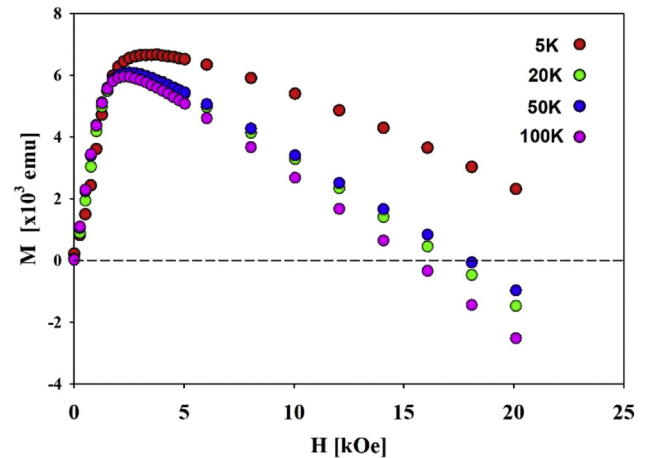


Fig. 9. Magnetization as a function of the applied magnetic field for sample $x = 1/4$ and $T = 5, 20, 50$ and 100 K.

$$M(H, T) = M_S L + \chi \quad (1)$$

where L is the Langevin function, defined as:

$$L = \tanh(x)^{-1} - 1/x; \quad x = \mu H / K_B T \quad (2)$$

μ is the mean effective magnetic moment, K_B is the Boltzmann constant ($= 1.38 \times 10^{-16}$ erg/K), M_S is the magnetic saturation and χ

is the diamagnetic component. The results are shown in Fig. 10.

The fitted parameters M_S , μ and χ are given in Table 4 and represented in Fig. 11. It can be observed that M_S and χ are nearly constant as a function of T whereas the mean effective magnetic moment μ increases from 5 to 25 K and then remains also constant, which is consistent with the behavior of $\chi(T)$ measurements.

The obtained value of the mean effective magnetic moment must be compared with the effective magnetic moment of Ta^{2+}

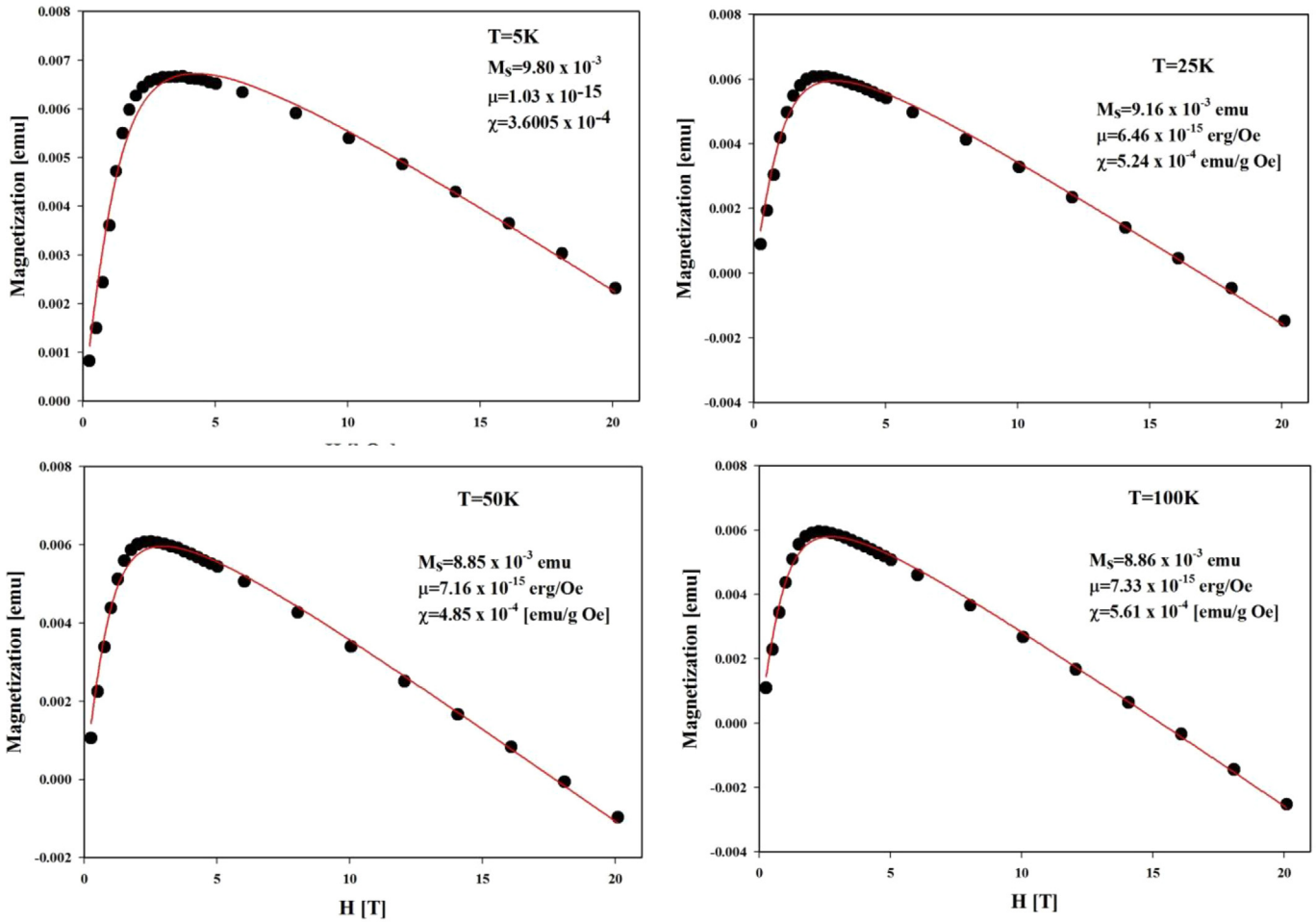


Fig. 10. Fitting of the $M(H,T)$ curves for sample $x = 1/4$ with the equation $M(H, T) = M_s L + \chi_D$ (see text).

Table 4
Fitted parameters of Fig. 11 curves.

T [K]	M_s [emu] $\times 10^{-3}$	χ [emu/gOe] $\times 10^{-4}$	μ [erg/Oe] $\times 10^{-15}$	$(\mu/\mu_B) \times 10^5$
5	9.80	3.60	1.03	1.11
25	9.16	5.24	6.46	6.97
50	8.85	4.85	7.16	7.72
100	8.86	5.61	7.33	7.91

since it has been assumed that two Ta-atom substitutes a pair Cu+In atoms in order to maintain the balance of the valence electrons and stoichiometry. The effective magnetic moment (μ_{eff}) of Ta^{2+} can be easily calculated using Hund's rules and the well-known equations derived from the Quantum Theory of Paramagnetism [64]:

$$\mu_{\text{eff}} = g \sqrt{J(J+1)} \quad (3)$$

and

$$g = 1 + \frac{J(J+1) + S(S+1) - L(L+1)}{2J(J+1)} \quad (4)$$

where g is the spectroscopic splitting factor or g -factor, and J , L and S are the quantum numbers. The electronic structure of Ta is $[\text{Xe}] 4f^{14}5d^36s^2$, so for Ta^{2+} is $[\text{Xe}] 4f^{14}5d^3$. Applying Hund's rules we obtain that $\mu_{\text{eff}}(\text{Ta}^{2+}) = 3.8 \mu_B$. The values obtained from the fit (in

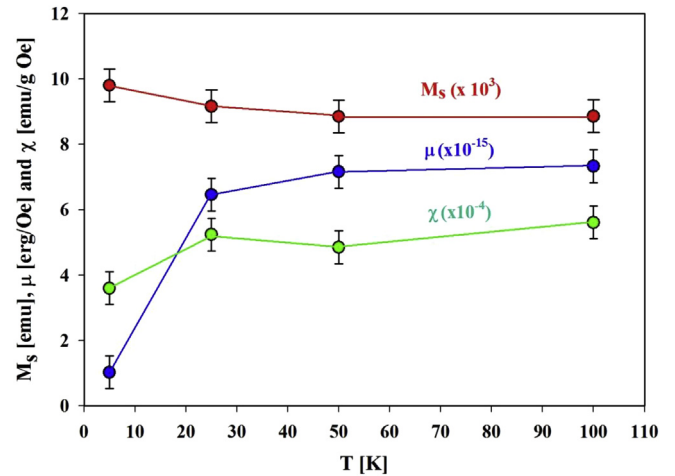


Fig. 11. Fitted values of M_s , μ and χ for sample $x = 1/4$.

μ_B units) are given in column five of Table 4; they are $\sim 10^5$ higher indicating that each cluster contains 0.3×10^5 , 1.8×10^5 , 2.0×10^5 , and 1.9×10^5 Ta-atoms, for $T = 5, 25, 50$ and 100 K respectively.

Certainly, the most probable oxidation states for Ta are Ta^{+3} , Ta^{+4} and Ta^{+5} , but in any case, the order of magnitude for μ_{eff} obtained from equations (3) and (4) are the same.

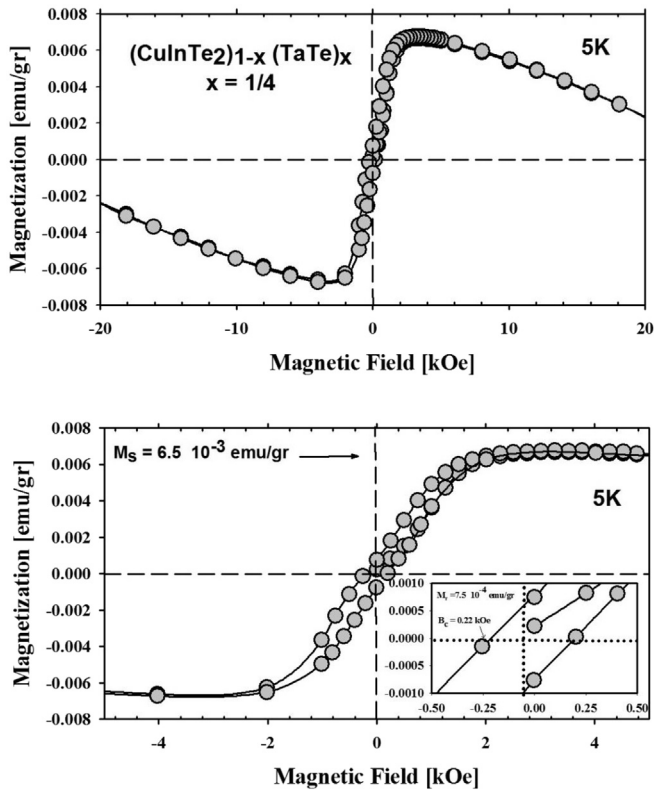


Fig. 12. $M(T, H)$ for sample $x=1/4$ at 5 K. In the top the complete curves up to $H=20$ kOe. In the bottom, the $M(T, H)$ curves, for low values of the applied magnetic field. In the inset an amplification of the region near $H=0$.

In Fig. 12, the same M Vs H curve, for $T=5$ K, is presented for low values of the applied magnetic field in order to visualize and obtain the magnetic saturation (M_s), the coercitive field (H_c) and the magnetic remanence (M_r) parameters, which are and represented in Fig. 13 and given in Table 5 (see also Fig. 14).

The vales of M_s obtained from the fit of Fig. 10 compared with those obtained from Fig. 12 have a difference of about 30%. This difference comes from the relative inaccuracy in the fit with eq. (1) and for the non-null contribution of the diamagnetic component to curves of Fig. 12 at low applied magnetic fields. Another interesting

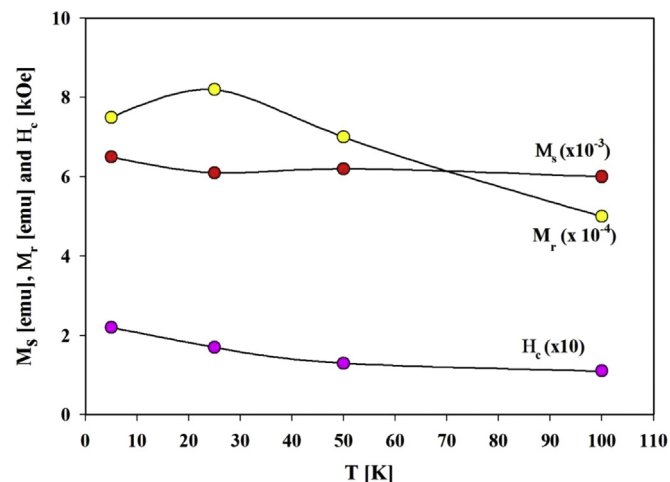


Fig. 13. The experimental values of M_r , M_s and H_c for sample $x=1/4$ at $T=5, 25, 50$ and 100 K. The error bars are lower than the size of the points.

Table 5

Values of the magnetic saturation (M_s), the coercitive field (H_c) and the magnetic remanence (M_r) for sample $x=0.25$ at $T=5, 25, 50$ and 100 K.

T[K]	M_s [emu] $\times 10^3$	M_r [emu] $\times 10^4$	H_c [kOe]	M_r/M_s
5	6.5	7.5	0.22	0.115
25	6.1	8.2	0.17	0.134
50	6.2	7.0	0.13	0.112
100	6.0	5.0	0.11	0.083

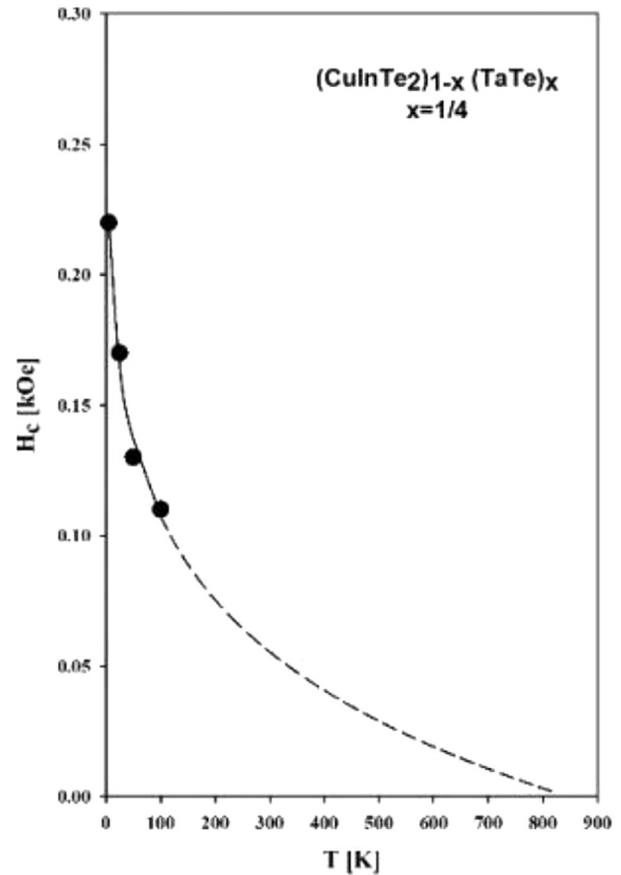


Fig. 14. Fit of H_c Vs T for sample $x=1/4$. Solid line: fit with equation (5). Dashed line: calculated extrapolation with parameters obtained from the fit.

parameter is the remanence ratio (M_r/M_s). For a uniaxial material in which each grain has a single easy axis and in which the grains are randomly oriented, the remanence ratio must be 0.5; however, the formation of free poles at the grain boundaries reduces considerably the remanence ratio [65]. In our case, the remanence ratio has values from 0.083 to 0.134 indicating the presence of the former effect.

The coercitive field values as a function of temperature have been fitted with the equation:

$$H_c = H_{c0} \left(1 - \frac{T}{T_B}\right)^n \quad (5)$$

where H_{c0} is the coercitive field at $T=0$ K and T_B is the blocking temperature at which $H_c=0$. The fitted parameters were $H_{c0}=0.51$ kOe, $T_B=845$ K and $n=0.11$. Theoretically, for particles of constant size, $n=1/2$ [66], but our value of 0.11 is in agreement with the magnetic susceptibility curves which don't have a unique peak in the ZFC curve indicating a system of particles with a

continuous distribution of sizes.

4. Conclusions

This work is part of a systematic investigation of $(\text{I-III-VI}_2)_{1-x}(\text{TM-VI})_x$ alloys, where TM is a transition metal. In this opportunity we are studied the $(\text{CuInTe}_2)_{1-x}(\text{TaTe})_x$ system. Samples were prepared by the melt and anneal technique and characterized by XRD, SEM, DTA and SQUID techniques. It was found that the solid solubility of TaTe in the $(\text{CuInTe}_2)_{1-x}(\text{TaTe})_x$ alloys system is around 10%; however only a mean tetragonal chalcopyrite-like phase and traces secondary phases have been observed by XRD up to $x = 2/3$. One of this secondary phases (Ta_2Te_3) could be identified by XRD, and other secondary phases have been identified by SEM: $\text{Cu}_2\text{Ta}_3\text{Te}_5$ which has not been reported before, $\text{CuTa}_2\text{InTe}_4$ which correspond to $x = 2/3$ of the $(\text{CuInTe}_2)_{1-x}(\text{TaTe})_x$ system but observed in compositions $x = 1/4$ and $x = 1/5$; and the oxides $\text{Ta}_{2.32}\text{O}_{7.40}$ and $(\text{TaTe})_2\text{O}_6$. The presence of the oxides is indicative of some contamination during the preparation process. Carefully examination of diffraction patterns gives indication that, in reality, the tetragonal phase is composed by two tetragonal phases with very close lattice parameters. We are interpreted this result as a spinodal nanodecomposition in two phases, one Ta-rich and another Ta-poor. However, it is also possible that samples are simply composed by two phases, without spinodal decomposition. To elucidate this controversy, it is necessary to obtain best quality samples, free of defects, and electron microscopy (TEM) measurements. We will try to perform these experiments in the next future. DTA measurements show a complicated thermal behavior of the samples with successive thermal transitions and wide liquid + solid regions suggesting a complicated phase diagram. Regarding to the magnetic properties, samples $x = 1/8, 1/7, 1/6, 1/5, 1/4$ and $1/2$ present a similar behavior, FC and ZFC curves show the hysteresis typical of systems composed by magnetic clusters. The samples contain two magnetic components, one paramagnetic (or superparamagnetic) and another ferromagnetic with $T_C > 300$ K. From fits of the M vs H curves, they were obtained values of the mean effective magnetic moment in the order of $\sim 10^5 \mu_B$, i.e. the clusters are composed by thousands of Ta-atoms. Composition $x = 2/3$ differs in the magnetic behavior from the others samples. Although there are also two magnetic components, one paramagnetic and another ferromagnetic, the ferromagnetic component orders at $T_C \sim 50$ K.

Acknowledgments

The authors want to thanks to Joseph Le Lannic, Isabelle Péron and Francis Gouttefangeas, Center de Microscopie Electronique à Balayage et MicroAnalyse (CMEBA), Université de Rennes (France) for SEM measurements; and Dr. D. Fiorani, Università di Roma (Italy) for SQUID experiments.

References

- [1] T. Dielt, D.D. Awschalom, M. Kaminska, H. Ohno (Eds.), *Spintronics (Semiconductors and Semimetals)*, vol. 82, Academic Press, Elsevier, 2008.
- [2] T. Dielt, H. Ohno, F. Matsukura, J. Cibert, D. Ferrand, *Science* 287 (2000) 1019.
- [3] G.A. Medvedkin, T. Ishibashi, T. Nishi, K. Hayata, Y. Hasewaga, K. Sato, *Jpn. J. Appl. Phys.* 39 (2000) L949–L951.
- [4] S. Cho, S. Choi, G.-B. Cha, S.C. Hong, Y. Kim, Y.-J. Zhao, A.J. Freeman, J.B. Ketterson, B.J. Kim, B.-C. Choi, *Phys. Rev. Lett.* 88 (2002), 257203.
- [5] S. Cho, J. Cho, S.C. Hong, S.J. Cho, *Korean Phys. Soc.* 42 (2003) S739–S741.
- [6] R.V. Demin, L.I. Koroleva, S.F. Marenkin, S. Mikhailov, T. Aminov, H. Szymczak, R. Szymczak, M. Baran, *J. Magn. Magn. Mater.* 290/291 (2005) 1379.
- [7] L.I. Koroleva, V.Yu Pavlov, D.M. Zashchirinskiĭ, S.F. Marenkin, S.A. Varnavskii, R. Szymczak, V. Dobrovolskii, L. Killanskiĭ, *Phys. Solid State* 49 (2007) 2121.
- [8] L.I. Koroleva, D.M. Zashchirinskiĭ, T.M. Khapaeva, S.F. Marenkin, I.V. Fedorchenko, R. Szymczak, B. Krzumanska, V. Dobrovolskii, L. Killanskiĭ, *Phys. Solid State* 51 (2) (2009) 303–308.
- [9] L. Kilanski, M. Gorska, V. Domukhovski, W. Dobrowolski, J.R. Anderson, C.R. Rotundu, S.A. Varniavskii, S.F. Marenkin, *Acta Phys. Pol.* 114 (2008) 1151–1157.
- [10] A.V. Kochura, R. Laiho, A. Lashkul, E. Lähderanta, M.S. Shakhov, I.S. Zakharov, S.F. Marenkin, A.V. Molchanov, S.G. Mikhailov, G.S. Jurev, *J. Phys. Condens. Mater.* 20 (2008) 1–5.
- [11] L.-J. Lin, N. Tabatabaie, J.H. Wernick, G.W. Hull, B.J. Meagher, *Elect. Mater.* 17 (1988) 321–324.
- [12] P.M. Shand, P.A. Polstra, I. Miotkowski, B.C. Crooker, *J. Appl. Phys.* 75 (10) (1994) 5731–5733.
- [13] N. Tsuji, H. Kitazawa, G. Kido, *Phys. Stat. Sol. A* 189 (3) (2002) 951–954.
- [14] J. Yao, B.W. Rudyk, C.D. Brunetta, K.B. Knorr, H.A. Figure, A. Mar, J.A. Aitken, *Mater. Chem. Phys.* 136 (2012) 415–423.
- [15] J. Yao, C.D. Brunetta, J.A. Aitken, *J. Phys. Condens. Matter* 24 (2012), 086006.
- [16] J. Yao, C.N. Kline, H. Gu, M. Yan, J.A.J. Aitken, *Solid State Chem.* 182 (2009) 2579–2586.
- [17] R.V. Demin, L.I. Koroleva, S.F. Marenkin, V.M. Novotortsev, B.M. Trukhan, S.A. Varnavskii, T.G. Aminov, G.G. Shabuninab, R. Szymczak, M. Baranc, *Heterogeneous magnetic state in Mn-doped CdGeP₂ and CuGaTe₂*, in: *Proc. 3rd Moscow Int. Symp. on Magnetism*, 2005.
- [18] S. Schorr, R. Hoehne, D. Spemann, Th Doering, B.V. Korzun, *Phys. Stat. Sol. A* 203 (11) (2006) 2783–2787.
- [19] V.M. Novotortsev, G.G. Shabuninab, L.I. Koroleva, T.G. Aminov, R.V. Demin, S.V. Boichuk, *Inorg. Mater.* 43 (1) (2007) 12–17.
- [20] P. Grima-Gallardo, F. Alvarado, M. Muñoz, S. Durán, M. Quintero, L. Nieves, E. Quintero, R. Tovar, M. Morocoima, M.A. Ramos, *Phys. Stat. Sol. A* (2012) 1–3.
- [21] S. Torres-Cuenza, P. Grima-Gallardo, M. Muñoz, S. Durán, M. Quintero, L. Nieves, R. Tovar, *Acta Cient. Venez.* 66 (1) (2015) 56–59.
- [22] M.A. Villarreal, P. Grima-Gallardo, M. Quintero, E. Moreno, E. Calderón, G.E. Delgado, P. Silva, J. Villegas, *Acta Cient. Venez.* 66 (3) (2015) 145–151.
- [23] M.A. Villarreal, P. Grima-Gallardo, M. Quintero, E. Moreno, G.E. Delgado, J. Fernández, P. Silva, J. Villegas, *Rev. LatinAm. Metal. Mater.* 32 (2) (2012) 292–298.
- [24] P. Grima-Gallardo, M. Soto, O. Izarra, L. Nieves, M. Quintero, G.E. Delgado, H. Cabrera, I. Zumeta-Dubé, A. Rodríguez, J.R. Glenn, J.A. Aitken, *Rev. LatinAm. Metal. Mater.* 37 (2) (2017) 83–92.
- [25] P. Grima-Gallardo, O. Izarra, R. Peña, M. Muñoz, S. Durán, M. Quintero, E. Quintero, H. Romero, *Rev. Cuba Fis.* 32 (1) (2015) 1–6.
- [26] P. Grima-Gallardo, E. Calderón, M. Muñoz-Pinto, S. Durán-Piña, M. Quintero, E. Quintero, M. Morocoima, G.E. Delgado, H. Romero, J.M. Briceño, J. Fernández, *Phys. Stat. Sol. A* 205 (7) (2008) 1552–1559.
- [27] Y.-J. Zhao, A. Zunger, *Phys. Rev. B* 69 (2004), 104422.
- [28] Y.-J. Zhao, A. Zunger, *Phys. Rev. B* 69 (2004), 075208.
- [29] A.V. Kochura, S.V. Ivanenko, A. Lashkul, E.P. Kochura, S.F. Marenkin, I.V. Fedorchenko, A.P. Kuzmenko, E.J. Lahderanta, *Nano Electron. Phys.* 5 (2013) 04013–04016.
- [30] L. Kilanski, W. Dobrowolski, R. Szymczak, E. Dynowska, M. Wójcik, N. Romcevic, I.V. Fedorchenko, S.F. Marenkin, *Sci. Sinter.* 46 (2014) 271–281.
- [31] J.A. Aitken, G.M. Tsoi, L.E. Wenger, S.L. Brock, *Chem. Mater.* 83 (2007) 1809.
- [32] T. Hwang, H. Ohno, F. Matsukura, *Phys. Rev. B* 63 (2001), 195205.
- [33] T. Katamani, H.J. Akai, *Superconductivity* 16 (2003) 95–97.
- [34] T. Katamani, H.J. Akai, *Mater. Sci. Semicond. Process.* 6 (2003) 389–391.
- [35] Zhao Y-Jun, A. Zunger, *Phys. Rev. B* 69 (2004), 104422.
- [36] P. Mahadevan, A. Zunger, *Phys. Rev. Lett.* 88 (2001), 047205.
- [37] H. Akai, *Phys. Rev. Lett.* 81 (1998) 3002.
- [38] D. Dietl, *J. Phys. Condens. Matter* 19 (2007), 165204.
- [39] P. Grima-Gallardo, S. Durán, M. Muñoz, M. Quintero, G. Delgado, J.M. Briceño, H. Romero, V. Briceño, J. Ruiz, J. Fernández, *Rev. Mexic. Fisica S* 53 (2007) 256.
- [40] G.E. Delgado, A.J. Mora, S. Durán, M. Muñoz, P. Grima-Gallardo, *J. Alloys Compd.* 439 (2007) 346.
- [41] Powder Cell for windows version 2.4. Klaus W. and Nolze N. Federal Institute for Materials Research and Testing, Berlin, Germany.
- [42] K.S. Knight, *Mater. Res. Bull.* 27 (1992) 161.
- [43] P. Grima-Gallardo, M. Muñoz, S. Durán, G.E. Delgado, M. Quintero, J. Ruiz, *Mater. Res. Bull.* 42 (2007) 2067.
- [44] P. Grima-Gallardo, S. Torres, M. Quintero, L. Nieves, E. Moreno, G.E. Delgado, *J. Alloys Compd.* 630 (2015) 146–150.
- [45] A. Boultif, D. Louer, *J. Appl. Cryst.* 37 (2004) 724–731.
- [46] <http://periodictable.com/Properties/A/CovalentRadius.html>.
- [47] <https://environmentalchemistry.com/yogi/periodic/covalentradius.html>.
- [48] https://www.webelements.com/periodicity/covalent_radius/.
- [49] https://chem.libretexts.org/Reference/Reference_Tables/Atomic_and_Molecular_Properties/A3%3A_Covalent_Radii.
- [50] <http://www.rsc.org/suppdata/cp/c0/c0cp01498b/c0cp01498b.pdf>.
- [51] <http://www.wiredchemist.com/chemistry/data/metallic-radii>.
- [52] E. Riedel, K. Ereku, S.Z. Yüksel, *Anorg. Allg. Chem.* 465 (1980) 131–140.
- [53] G.E. Delgado, J.A. Mora, P. Grima-Gallardo, S. Durán, M. Muñoz, M. Quintero, *Chalcogenide Lett.* 6 (8) (2009) 335–338.
- [54] M. Conrad, B.J. Harbrecht, *Alloys Compd.* 187 (1) (1992) 181–192.
- [55] P. Lavela, M. Conrad, A. Mrotzek, B. Harbrecht, J.L. Tirado, *J. Alloys Compd.* 282 (1999) 93–100.
- [56] G.E. Delgado, A.J. Mora, P. Grima-Gallardo, M. Muñoz, S. Duran, M. Quintero,

- Phys. B Condens. Matter 403 (2008) 3228.
- [57] V.I. Khitrova, V.V. Klechkovskaya, Sov. Phys. Crystallogr. 25 (1980) 669–672.
- [58] P. Villars, K. Cenzual (Eds.), Structure Types. Part 3: Space Groups (194) P63/mmc - (190) P-62c. Landolt-Börnstein - Group III Condensed Matter (Numerical Data and Functional Relationships in Science and Technology), vol 43A3, Springer, Berlin, Heidelberg, 2006.
- [59] J.A. Alonso, A. Castro, E. Gutiérrez Puebla, M.A. Monge, I. Rasines, C. Ruiz Valero, J. Solid State Chem. 69 (1987) 36–42.
- [60] M. Gaitán, A. Jérez, C. Pico, M.L. Veiga, Mater. Res. Bull. 22 (4) (1987) 477–481.
- [61] L. Loubbidi, A. Chagraoui, B. Orayech, M. Naji, A. Tairi, A. Moussaoui, O. Ait Sidi Ahmed, I. Yakine, J.M. Igartua, Verres Ceramiques Compos. 4 (1) (2015) 7–14.
- [62] L.S. Palatnik, E.I. Rogacheva, Sov. Phys. Tech. Phys. 12 (5) (1967) 503.
- [63] P. Weiss, Compt. Rend. 143 (1906) 1136–1139.
- [64] B.D. Cullity, C.D. Graham, Introduction to Magnetic Materials, second ed., IEEE Press. Wiley, USA, 2009, pp. 100–102.
- [65] B.D. Cullity, C.D. Graham, Introduction to Magnetic Materials, second ed., IEEE Press. Wiley, USA, 2009, p. 328.
- [66] B.D. Cullity, C.D. Graham, Introduction to Magnetic Materials, second ed., IEEE Press. Wiley, USA, 2009, p. 388.